Experimental and theoretical investigation of the boiling heat transfer in a low pressure natural circulation system

Viereckl, F.; Schleicher, E.; Schuster, C.; Lippmann, W.; Hurtado, A.;

Originally published:

July 2019

Experimental and Computational Multiphase Flow 1(2019)4, 286-299

DOI: https://doi.org/10.1007/s42757-019-0023-0

Experimental and theoretical investigation of the boiling heat transfer in a low pressure natural circulation system

Frances Viereckl[1], Eckhard Schleicher[2], Christoph Schuster[1], Wolfgang Lippmann[1], Antonio Hurtado[1]

[1] Chair of Hydrogen and Nuclear Energy, Technische Universität Dresden

George-Bähr-Str.3, 01069, Dresden, Germany

[2] Experimental Thermal Fluid Dynamics, Helmholtz-Zentrum Dresden-Rossendorf

Bautzner Landstraße 400, 01328, Dresden, Germany

Email: frances.viereckl@tu-dresden.de

Abstract

The implementation of passive safety systems in nuclear reactors provide the opportunity to enhance the nuclear safety. On the other hand, an accurate and reliable prediction of the heat removal behavior is not ensured because the operating conditions of certain types of passive systems like containment cooling systems differ from the validity ranges of the established heat transfer correlations. Therefore, a generic and detailed investigation is still necessary for passive systems.

Against this background, the test facility GENEVA was erected at Technische Universität Dresden in 2012. Since the commissioning, generic experiments concerning the system and stability behavior of this facility, which emulates a low pressure and low flow (LPLF) natural circulation system, were provided. Nevertheless, the investigation of the heat transfer behavior remained an open issue. On this account, the instrumentation in the heat transfer region inside GENEVA was improved to gather the necessary temperature and void fraction profiles.

The performed experiments provide a generic and wide database concerning boiling in a LPLF natural circulation systems. Within this paper, the development of the wall and bulk fluid temperature as well as the axial and center line void fraction profile in a slightly inclined tube for different heat flow rates are discussed. Furthermore, flow patterns could be identified on behalf of the void fraction measurements. To conclude the experimental analysis, the development of the heat transfer coefficient was estimated.

These experimental data provide the basis for a simulation with the lumped-parameter thermal-hydraulic code ATHLET and serve as validation reference. However, the comparisons between the experimental and computational results show insufficient agreements. Mainly, the simulation misses the saturation point of the experiments, which leads to great differences of the void fraction values. Moreover, inaccuracies appear as well with the heat transfer coefficient.

The experimental and computational results that are discussed in this paper provide the basis for the advancement not only of heat transfer correlations but also of flow pattern maps within the range of low pressure natural circulation system. In summary, this investigation contributes to the general purpose to enhance nuclear safety by providing an accurate and reliable prediction of the heat removal capacity of passive systems.

Keywords

flow patterns, GENEVA, heat transfer coefficient, low pressure natural circulation, nuclear safety, passive systems

1 Introduction

In an increasing amount of nuclear new builds, passive systems are implemented to enhance nuclear safety, because these systems are able to remove heat without intervention or the supply of external energy. The last link in the heat removal chain in such a passive safety system is the heat removal from the containment to the ultimate heat sink (e. g. atmosphere or cold water pool). For realizing these containment cooling systems in nuclear reactors, different concepts were developed and schematically represented in Figure 1:

A air/steam heat exchanger at the containment ceiling connected to a water pool on the containment,
B air/steam heat exchanger in the upper part of the containment connected to a water heat exchanger inside an external elevated water pool,
C external steam condenser heat exchanger inside an external elevated water pool,
D containment structures, which function as air/steam – air heat exchanger with a secondary chimney effect [1].

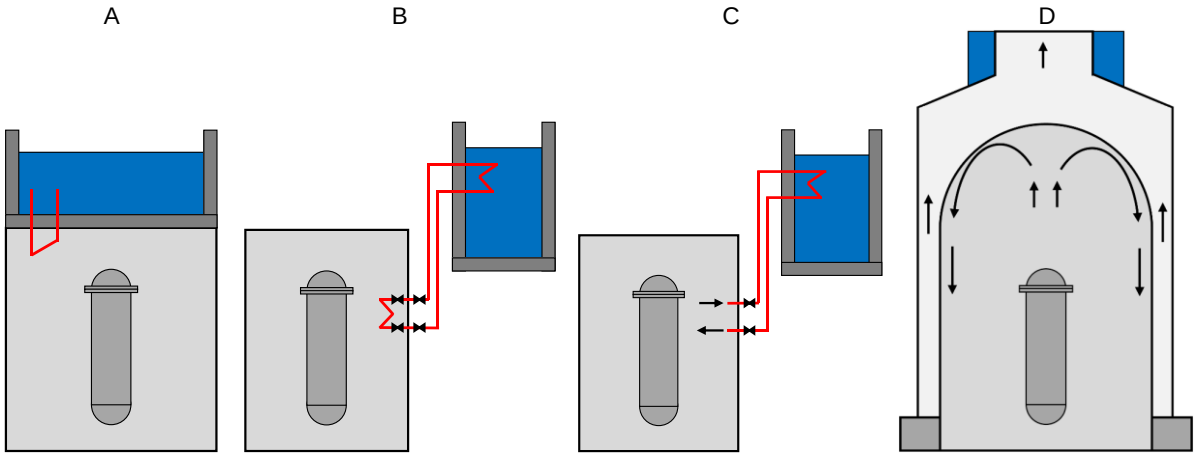

Figure 1: Schematic representation of the different concepts for containment cooling systems (A – air/steam heat exchanger connected with a water pool at the top of the containment, B – air/steam heat exchanger connected with a water heat exchanger inside an external water pool, C – external steam condenser heat exchanger inside an external water pool, D – containment structures functioning as air/steam - air heat exchanger) [1]

In general, these systems consist of a heat exchanger, which is located in the upper part of the containment or directly connected to the containment, the geodetically elevated heat sink and connecting tubes. Due to the heat transfer from the containment, the fluid inside this described loop heats up, which leads to a decrease of the density. With a sufficient height difference between heat source (containment) and heat sink (e. g. atmosphere or cold water pool), a natural circulation evolves. By reaching saturation conditions, the fluid starts boiling and different flow patterns can develop in the two-phase natural circulation flow [1].

To design or apply these containment cooling systems for safety related functions in nuclear power plants, an accurate and reliable prediction of the removable heat flow is crucial. Since heat transfer surface and temperature difference can be determined precisely, the critical parameter is the boiling heat transfer coefficient from the heated wall to the fluid.

One approach to define the operational and heat transfer behavior and thus to determine the removable heat flow is the simulation applying thermal-hydraulic system codes. For calculating the heat transfer coefficient during boiling, these codes refer to established correlations, which are each validated within a certain parameter range. In [2], Manthey et al. already reviewed

and described correlations for the boiling heat transfer, which are implemented in thermal-hydraulic system codes. To obtain a first assessment of the capability of the implemented correlations to predict the operational behavior of passive containment cooling systems, the parameter range of the validation for these correlations regarding water is compared to the thermal-hydraulic conditions within the passive systems. Therefore, the range of validity of established heat transfer correlations for water is listed in Table 1.

Table 1: Validity range of established heat transfer correlations for water

Modified Chen correlation (cf. Eq. (4)), [3–6]	
geometry	tube, annulus
flow	upwards, downwards
pressure in bar	0.55 to 34.8
liquid inlet velocity in m/s	0.06 to 4.5
quality	0.01 to 0.71
heat flux in kW/m²	44 to 2,400
flow conditions	forced convection by pumps
McAdams correlation (cf. Eq. (5)and (6)), [7]	
tube diameter in m	0.05
pressure in bar	1.01325
fluid temperature in °C	30 to 50
wall temperature in °C	34 to 92
Dittus-Boelter correlation (cf. Eq. (7)), [8, 9]	
tube diameter in m	0.016
fluid temperature in °C	33.1 to 83.05
wall temperature in °C	98.83 to 99.56
linear velocity in m/s	0.27 to 5.94
heat flow rate in kW	11.66 to 27.66
McEligot correlation (cf. Eq. (8)), [10, 11]	
tube diameter in m	0.001
heated length in m	0.762
mass flow in kg/h	0.59 to 0.64
axial heat flux in W/m	3.7 to 199
surface temperature in °C	32.2 to 638.9

Complementary to the shown validity ranges, Table 2 presents an overview of the conditions of several passive systems, which are applied in nuclear reactors to remove the heat from the containment during an accident.

Table 2: Overview of conditions for several passive systems applied to remove heat from the containment in a nuclear power plant [1]

Containment cooling condenser, KERENA (concept I according to Figure 1)	
heat dissipation in MW	5.5
pressure in bar	2.5
heat exchanger type	inclined tube bundle
heat sink	elevated water pool
Passive containment cooling system, AP 1000 (concept IV according to Figure 1)	
pressure in bar	atmospheric
heat exchanger	containment vessel
heat sink	atmosphere

Containment passive heat removal system, VVER-1200 (concept II according to Figure 1)	
heat dissipation in MW	19
pressure in bar	2.6
heat exchanger	vertical tube bundle
heat sink	elevated water pool
Passive containment cooling system, SBWR, ESBWR (concept III according to Figure 1)	
heat dissipation in MW	11
pressure in bar	4.2
heat exchanger	vertical tube bundle
heat sink	elevated water pool

Summarizing the presented data in Table 2, following conditions for a containment cooling system emerge independently from their design:

- low pressure (atmospheric pressure plus the pressure of the water column),
- low heat flux and
- steam-heated natural circulation [1].

Associating these conditions to the presented validity ranges, only an insufficient overlap can be concluded. The experimental data for validating the Chen correlation were performed inside forced circulation loops with pumps. Regarding the McAdams correlation, the pressure as well as the temperature were lower than in the presented cooling systems. The temperatures of the experiments for the Dittus-Boelter correlation remained lower than the saturation temperatures. The experiments for the McEligot correlation were performed in microchannels. This comparison indicates that the validation within the range of the presented natural circulation systems is incomplete. Therefore, the investigation concerning the boiling heat transfer in LPLF natural circulation systems has to be extended. On this account, further experiments, which incorporate all operating conditions of passive containment cooling systems, have to be performed and analyzed numerically.

This paper focuses on the boiling heat transfer in the passive system containment cooling condenser, which is implemented in the boiling water reactor design KERENA. The experimental data are provided at the test facility GENEVA, which models this containment cooling system and is described in chapter 2. The numerical investigation is performed by simulations with the system code ATHLET.

2 Experimental and computational setup

2.1 Test facility GENEVA

In 2012, Cloppenborg et al. set up the test facility GENEVA to investigate the system and stability behavior of the passive containment cooling condenser (cf. Figure 1, A) [12]. GENEVA represents a heat removal system with single- or two-phase natural circulation and is heated by saturated steam.

Functional principle

The test facility consists of three circuits. Figure 2 displays these three circuits with their interfaces and the operating principle of the facility schematically by a simplified process flow diagram.

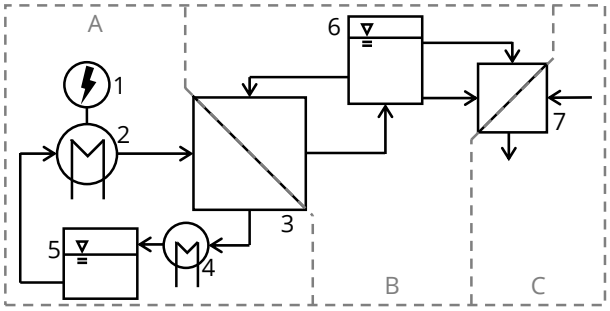

Figure 2: Simplified process flow diagram of the test facility GENEVA with the heat source circuit (A), test circuit (B) and cooling circuit (C)

The heat source circuit (Figure 2, A) provides saturated steam by two electrically heated evaporators. The test circuit (Figure 2, B) represents a natural circulation loop connecting the heat source with the elevated heat sink. With the cooling circuit (Figure 2, C) generic investigations by providing stationary measuring points are enabled.

The investigated boiling heat transfer occurs inside the tube of the heat exchanger that interfaces the heat source circuit and test circuit. This heat exchanger is located inside a steam chamber and is connected to an elevated water pool, which serves as heat sink, at the tube inlet and outlet. Figure 3 shows a simplified view into the steam chamber of the test facility GENEVA with its main components.

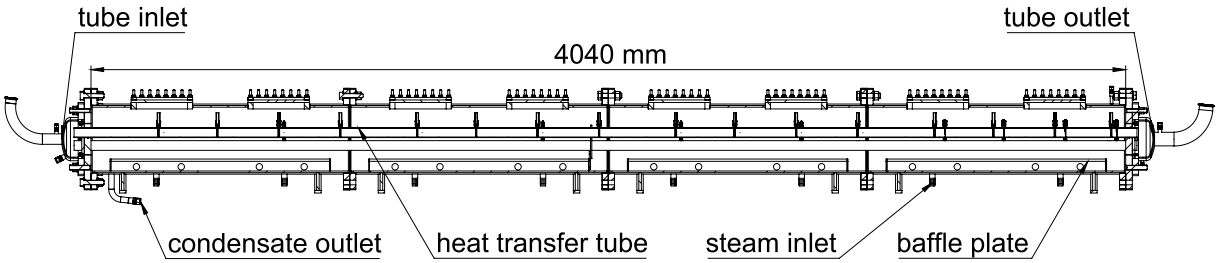

Figure 3: Simplified longitudinal view into the steam chamber of the test facility GENEVA

In the heat source circuit, the saturated steam from the evaporators is led into the steam chamber through eight nozzles (cf. Figure 3). To emulate the pool boiling conditions inside the containment, the steam flow is slowed down by baffle plates. The steam condenses at the outside of the tube and the latent heat is transferred to the test circuit. The temperature of the water inside the tube rises leading to a decrease of the density and to natural convection [13]. If saturation conditions are reached inside the tube, the water will start boiling and the single-phase natural convection will transit into a two-phase flow.

Instrumentation

Within the scope of the previous investigation, Cloppenborg et al. measured the mass flow inside the test circuit as well as the pressure and fluid temperature at the inlet of the heat transfer tube and the fluid temperature at the tube outlet. Regarding the heat source circuit,

the steam mass flow, the pressure inside the steam chamber and the steam temperature were measured parameters [13]. In order to analyze the heat transfer during the described boiling process, the instrumentation inside the steam chamber of the test facility GENEVA was improved to gather all necessary data. Additionally required parameters are the void fraction and fluid temperature inside the heat transfer tube as well as the wall temperature at the outside of the tube. On that account, 104 thermocouples were added in total measuring the axial and radial profile of the fluid temperature inside the heat transfer tube and the axial and azimuthal profile of the wall temperature at the outside of the tube. Regarding the void fraction, 16 linear conductivity sensor probes were implemented inside the heat transfer tube indicating the axial and center line void fraction profile. The according scales for the azimuthal profile (outside the tube) and center line profile (inside the tube) are illustrated in Figure 4.

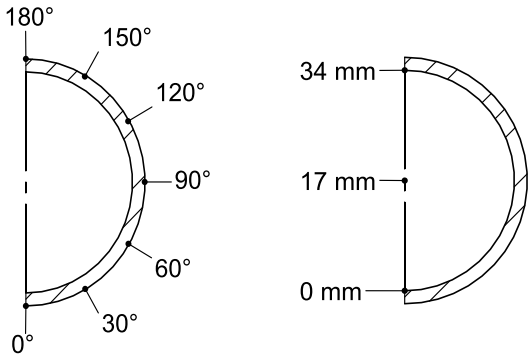

Figure 4: Scale for the azimuthal wall temperature (left) and center line void fraction (right) profile

Table 3 gives an overview of all measured parameters concerning the boiling heat transfer in the test facility GENEVA with the according measuring devices.

Table 3: Overview of the measured parameters regarding the boiling heat transfer at the test facility GENEVA

parameter	measuring device	profile
test circuit		
fluid temperature	48 thermocouples	axial radial
mass flow	1 Coriolis flow meter	-
pressure	1 pressure sensor	-
void fraction	16 linear conductivity sensor probes	axial center line
heat source circuit		
wall temperature	56 thermocouples	axial azimuthal
steam temperature	6 thermocouples	axial
steam mass flow	1 ultrasonic flow meter	-
pressure	1 pressure sensor	-

Further, the positions of the components, inner thermocouples and void probes are displayed in the simplified lateral view into the steam chamber of GENEVA in Figure 5.

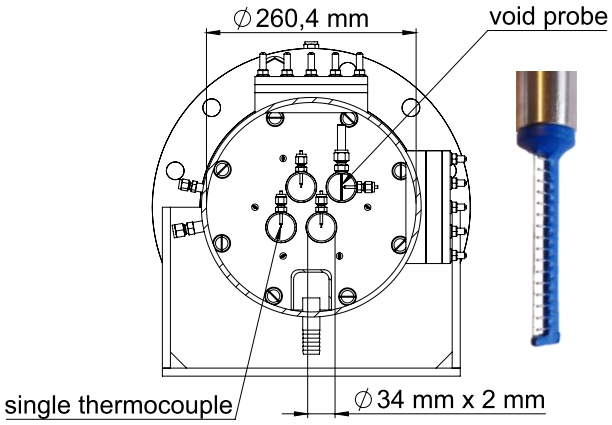

Figure 5: Simplified lateral view into the steam chamber of GENEVA (left) and detailed view of a void probe (right)

The displayed void probes in Figure 5 are custom-built multipoint conductivity sensors quantifying the local instantaneous void fraction. The probes consist of 16 single needles, which allow the measurement of the center line profile in 16 different heights, oriented against the flow direction for optimal penetration of bubbles and liquid films.

A thin 100 µm wire is stretched along the tube diameter in a small distance to the described needles and is connected to a transimpedance amplifier. The 16 needles are used as transmitting electrodes excited by a short (6 µs) bipolarity voltage pulse consecutively one by one. In case of water in between a single needle and the measuring wire, a current pulse is flowing towards the amplifier, while steam or gas interrupt the current flow. The 16 single probes, which are installed equidistantly along the tube are connected to a wire-mesh sensor [13] electronic system developed at HZDR with 16x16 channels. This setup allows the simultaneous sampling of all 16 probes and therefore of 256 measuring points for the void fraction inside the tube with a measurement frequency of up to 10,000 complete measurements per second for a time of 30 minutes maximum.

To quantify the void fraction by this recorded current, which represents the collected raw data $I^{\,\mathrm{meas}}_{x,y,z}$ (with the probe positon *x*, the height *y* and the frame *z*), the data are pre-processed by applying a void fraction calculation based on a full liquid calibration. Therefore, a calibration data set $I^{\mathrm{water}}_{x,y,z}$ for the completely water filled tube with as close as possible temperature and pressure conditions to the later experiment is required. By averaging these data over all measured sampling times, a two dimensional calibration matrix $\bar{I}^{\,\mathrm{water}}_{x,y}$ is created. Applying this calibration matrix for normalizing the experimental data, the local instantaneous void fractions $\alpha_{x,y,z}$ are calculated by Eq. (1).

$$\alpha_{x,y,z} = \frac{\bar{I}^{\,\mathrm{water}}_{x,y} - I^{\,\mathrm{meas}}_{x,y,z}}{\bar{I}^{\,\mathrm{water}}_{x,y}} = 1 - \frac{I^{\,\mathrm{meas}}_{x,y,z}}{\bar{I}^{\,\mathrm{water}}_{x,y}} \qquad (1)$$

It has to be mentioned that Eq. (1) [14] is applied for wire-mesh sensors and based on the assumption of a linear relation between the local gas holdup and the measured current, which is not completely correct for the given geometry of the probes. However, due to the stratified wavy flow structure in the tube section, a binary character of the data can be assumed. This means a single needle sensor describes either only steam (1) or only water (0). Thus, a binarization of the local instantaneous data with a certain threshold is recommended. By temporally averaging, characteristic local holdups and steam/water distributions can be

calculated. The uncertainty resulting from the assumption mentioned above is therefore negligible compared with measurement uncertainties from standard methods for local holdup measurements as gamma-ray densitometry or single tip needle probes, where an equal distribution of the void fraction along the pipe diameter has to be assumed (e.g. [15]).

To provide the void fraction in the cross-section of the tube based on the center line profile, an averaging assuming the stratification of the phases inside the tube is performed. Therefore, the cross-section is divided into 16 circular segment areas corresponding to positions of the single measuring points of the void probes. The ratio between the single circular segment area and the total cross-sectional area provides the proportional factor for the corresponding void fraction. The division of the tube cross-section into circular segment areas (cf. Figure 18) and the correlations for calculating the circular segment areas (cf. Eq. (9) to (12)) are presented in appendix B.

Operational parameters

Due to the thermal load and the comparability with the conditions in the containment, the maximal temperature outside the tube in the steam chamber is set to 140 °C. Due to the saturation conditions, the corresponding steam pressure can reach values up to 3.6 bar. Inside the tube, the bulk fluid temperature can rise up to 116 °C due to the design induced maximal pressure of 1.8 bar.

Concerning the experimental investigation of the boiling heat transfer, the results of three stationary measuring points at the test facility GENEVA are presented in section 3.1 of this paper. The stationary conditions are provided by a continuous steam supply and constant conditions in the steam chamber. Moreover, the temperature at the tube inlet maintained constant as a result from adjusting the heat removal by the cooling circuit. Table 4 presents the status parameter of the three experimental points, which are presented and analyzed in detail in section 3.1. Further, these parameter serve as input parameter of the simulation.

Table 4: Status parameter of the presented stationary measuring points

parameter	**1**	**2**	**3**
test circuit			
inlet temperature ϑ in °C	95.1	95.3	95.72
inlet pressure p in bar	1.41	1.36	1.39
inlet mass flow $\dot{m}$ in kg/s	0.35	0.38	0.37
outlet temperature ϑ in °C	107.3	106.9	107.8
outlet pressure p in bar	1.31	1.29	1.33
outlet void fraction α	0.35	0.58	0.56
heat source circuit			
inlet temperature ϑ in °C	124.9	126.1	128.2
inlet pressure p in bar	2.31	2.4	2.56
total inlet mass flow $\dot{m}$ in kg/s	0.007	0.009	0.011
heat flow rate Q in kW	**15.3**	**19.9**	**23.4**

2.2 ATHLET model of the heat transfer area

ATHLET (analysis of thermal-hydraulics of leaks and transients) is a one-dimensional code to analyze the thermal-hydraulic behavior during design basis and beyond design basis accidents in light water reactors. The code comprises two-phase fluid dynamic models based on the conservation equations. The simulation is performed in ATHLET because it contains the basic correlations for the boiling heat transfer [16]. Moreover, the code should be „capable to capture basic phenomena that are characteristic for the operation of passive systems“ [17], although

the validation solely bases on investigations of a passive high pressure system [18, 19]. On this account, the applicability of ATHLET for LPLF natural circulation systems has to be validated by further investigations.

To analyze the implemented models concerning the boiling heat transfer numerically, the steam chamber of the test facility GENEVA is emulated in ATHLET. Figure 6 displays the nodalization, i.e. the division in so-called thermo-fluiddynamic objects (TFOs) and control volumes (CVs), of the investigated area. To consider the steam heating besides of the heat transfer tube, two flow systems (in ATHLET: priority chains) according to the circuits of the test facility GENEVA are modelled. These systems with their respective TFOs are:

- heat source circuit: eight steam inlets, steam chamber, condensate outlet;
- test circuit: tube inlet, heat transfer tube, tube outlet.

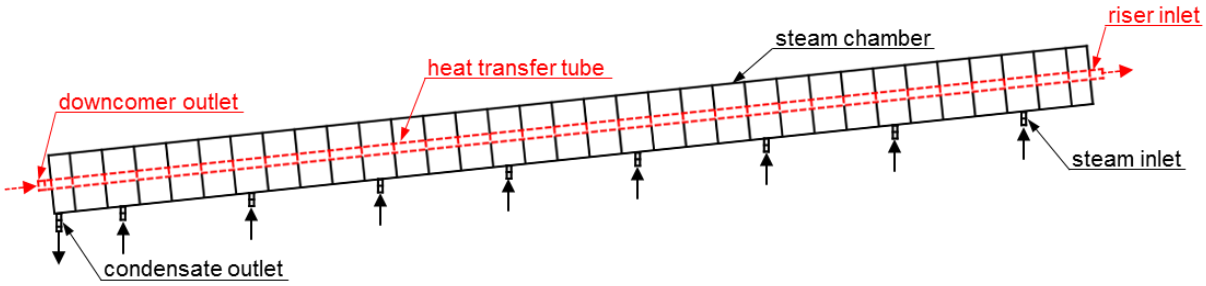

Figure 6: Nodalization of the steam chamber in ATHLET with the systems heat source circuit (black, solid line) and test circuit (red, dashed line) with their respective thermo-fluiddynamic objects and flow directions

The TFOs that model the inlets of both systems are provided with the command *fill*. Using this command, a flow with a user-defined mass flow and enthalpy is generated in this object. On the other hand, the outlet TFOs have a *time-dependent volume* (TDV) with a certain pressure and enthalpy, which are again user-defined. The values of the parameters concerning the fills and the TDVs comply with the experimental status parameters in Table 4 and are presented for each applied experimental point in Table 5.

Table 5: Values applied for the parameters inlet mass flow, inlet enthalpy, outlet pressure and outlet enthalpy in the simulation of the experimental points 1, 2 and 3

parameter	value		
	1	2	3
single steam inlet			
mass flow in kg/s	0.0009	0.0011	0.0013
enthalpy in kJ/kg	2,712.9	2,714.6	2,717.6
condensate outlet			
pressure in bar	2.31	2.40	2.56
enthalpy in kJ/kg	524.5	529.6	538.6
tube inlet			
mass flow in kg/s	0.35	0.38	0.37
enthalpy in kJ/kg	398.6	399.2	401.1
tube outlet			
pressure in bar	1.31	1.29	1.33
enthalpy in kJ/kg	450.9	450.7	454.4

To evaluate the performance of ATHLET concerning the predictability of the thermal-hydraulic behavior in LPLF passive containment cooling systems, the experimental data will be compared with the fluid dynamic data from the ATHLET simulation. The comparative parameters are the bulk fluid temperature, the steam void fraction and the heat transfer coefficient. To ensure that the effect of the heat transfer at the outside of the heat transfer tube is neglected, the measured outer wall temperatures will be applied as boundary condition.

3 Results and discussion

Regarding the investigation of the boiling heat transfer, the experimental results are presented initially. This includes the analysis of the wall and bulk fluid temperature profiles as well as void fraction profiles and in conclusion heat transfer coefficients. Following this, the presented data are discussed in comparison to the computational results from the ATHLET simulation.

3.1 Experimental results

To start the heat transfer analysis, the inner wall temperature $T_{w,i}$ is determined by heat conduction through the wall based on the measured outer wall temperature $T_{w,o}$ and the assumption of a uniform heat flux distribution (cf. Eq. (2)). Because of this assumption, the correlation for the linear heat flux q' can be applied to take no account of the tube length or axial position. Therefore, just the inner tube diameter D_i, outer diameter D_a and the heat conductivity of the employed steel k_{st} are required.

$$q' = \frac{2\,\pi\,k_{st}}{\ln(D_o/D_i)}\left(T_{w,o} - T_{w,i}\right) \qquad \textbf{(2)}$$

According to this, the azimuthal profiles of the inner wall temperature are provided at different axial positions. The diagrams in Figure 7 display the development of the inner wall temperature over the tube angle at the different axial positions for the three experimental points, which are presented in Table 4.

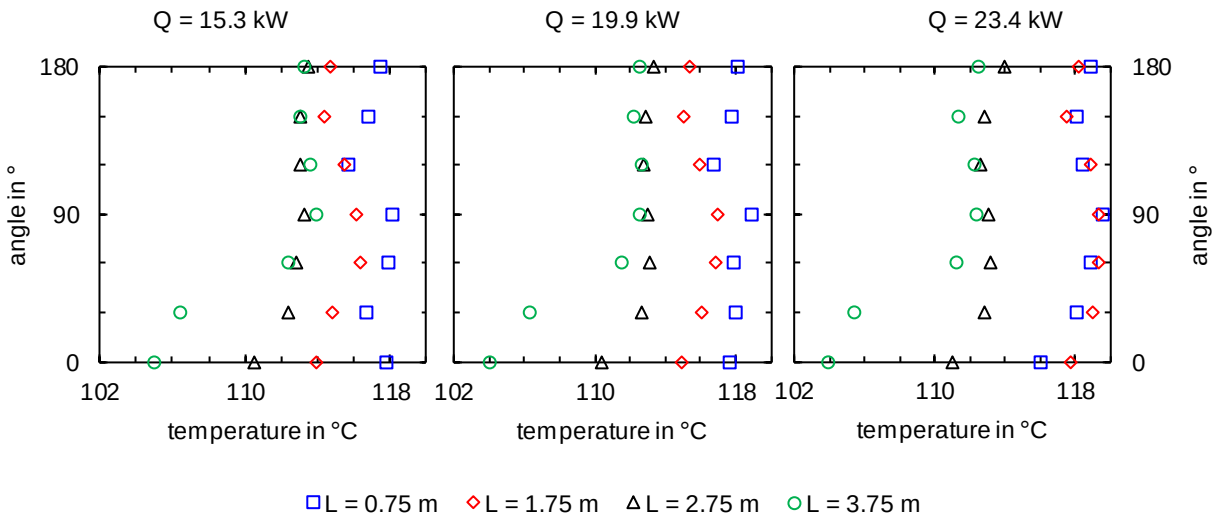

Figure 7: Development of the inner wall temperature with the tube angle at different axial positions for the experimental points 1 (left), 2 (middle) and 3 (right)

Near the tube inlet (L = 0.75 m), the wall temperature is evenly distributed. With further tube length, a temperature stratification in the lower third of the tube can be identified, which decreases with increasing heat flow rate due to the increasing mass flow. The diagrams in Figure 7 reveal also that the inner wall temperature decreases with increasing length.

In contrast to this development, the bulk fluid temperature, which is presented in Figure 8, increases with increasing tube length. The stagnation of the bulk fluid temperature in the fourth quarter of the tube can be referred to the attainment of saturation conditions. Comparing the three experimental points, the bulk fluid temperature is slightly increasing with increasing heat flow rate.

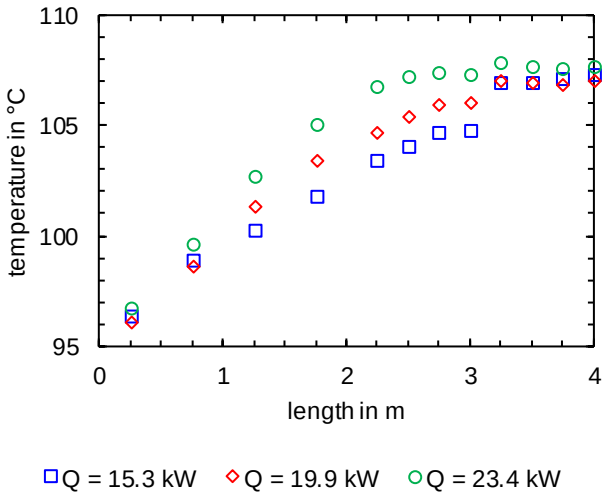

Figure 8: Development of the bulk fluid temperature with the tube length for the experimental points 1, 2 and 3

For the heat transfer analysis based on these data, the difference between the inner wall temperature and the bulk fluid temperature is determined (cf. Figure 9).

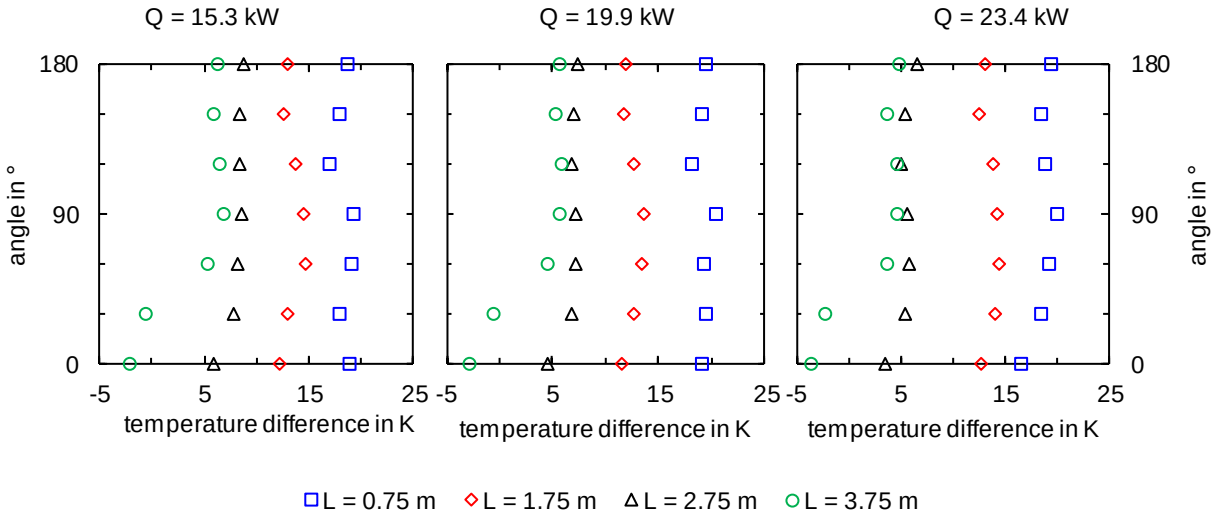

Figure 9: Development of the difference between the inner wall and bulk fluid temperature with the tube angle at different axial positions for the experimental points 1 (left), 2 (middle) and 3 (right)

The display of the temperature differences shows a decrease with increasing tube length. At the tube bottom (0° to 30°) and 3.75 m tube length, the wall temperature is even lower than

the bulk fluid temperature, whereby this tube section is not available for the heat transfer. Regarding the increase of heat flow, no significant distinctions within the values for the temperature difference are noticeable.

According to the presented temperature profiles, center line void fraction profiles at different axial positions and for different heat flow rates are displayed in Figure 10. The diagrams show that the start of nucleate boiling is closer to the tube inlet with increasing heat flow rate. Moreover, the void fraction increases with increasing tube length and with increasing heat flow rates.

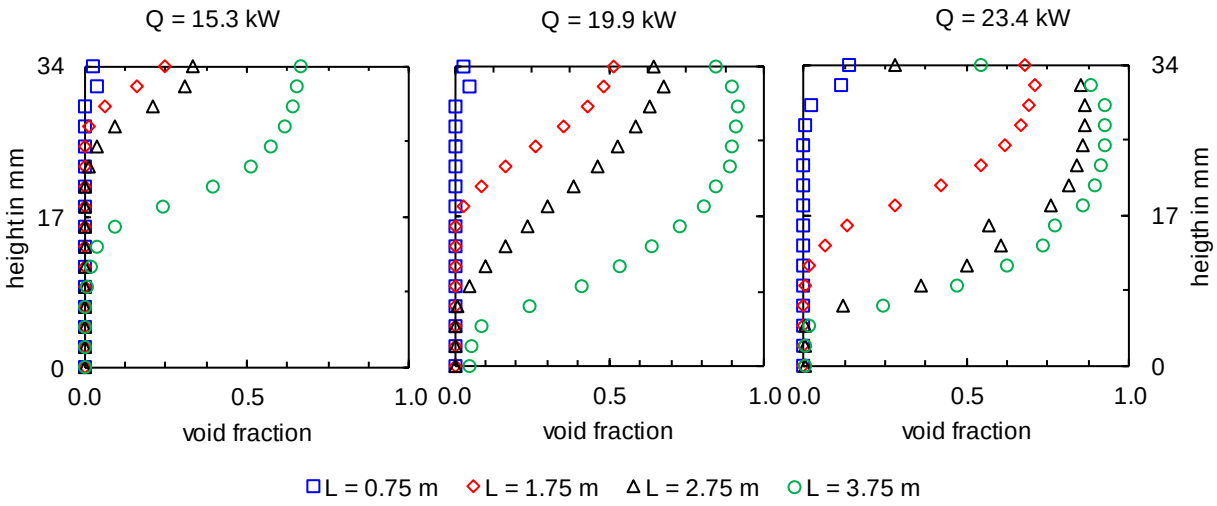

Figure 10: Development of the void fraction with the tube height at different axial positions for the experimental points 1 (left), 2 (middle) and 3 (right)

Beyond that, the void fraction data with higher values (Q = 19.9 kW and Q = 23.4 kW; L ≥ 2.75 m) show a decreasing trend at the top of the tube, which is caused by the inertia of the fluid at the tube wall and the probe needle (cf. section 2.1). Beside the development of the void fraction within the center line, the time curve of the void fraction, which is presented in Figure 11, is to be analyzed to obtain information regarding the two-phase flow behavior and flow patterns, which have a strong influence on the heat transfer [20].

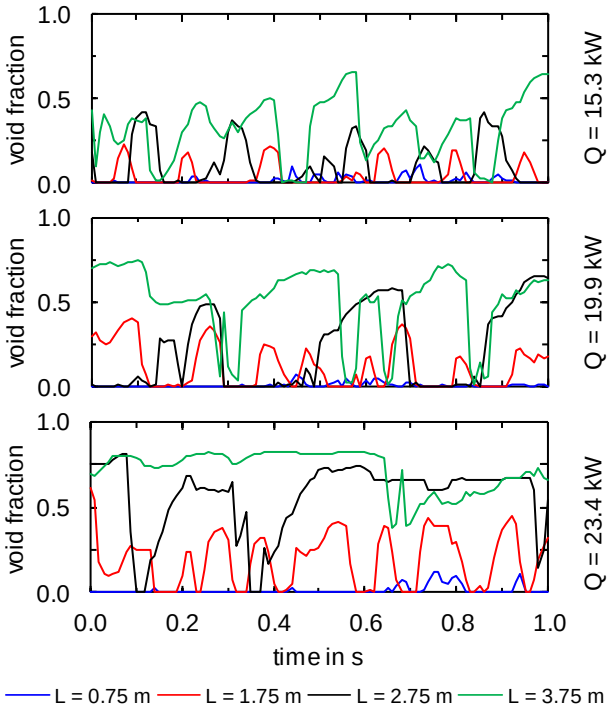

Figure 11: Time curve of the void fraction different axial positions of the heat transfer tube for the experimental points 1 (top), 2 (middle) and 3 (bottom)

The time curves in Figure 11 reveal different phenomena, which indicate several flow patterns alongside the tube. Regarding the curve at the length L = 0.75 m (blue line) and the heat flow rate Q = 15.3 kW, the formation of steam is irregular and leads to a mean void fraction of 0.013 as well as long periods, where no nucleation takes place. Within the next experimental points (Q = 19.9 kW, Q = 23.4 kW), the same irregular nucleation behavior with a slightly decreased mean void fraction of 0.006 and 0.018 is observable. Therefore, nucleate boiling can be assumed. The void fraction at the length L = 1.75 m (red line) within all experimental points shows a regular temporal course, whereas the mean and maximum value of the void fraction as well as the according frequency of the maxima increase with increasing heat flow rate. By reference to the maximum values for the void fraction from 0.223 (Q = 15.3 kW) to 0.619 (Q = 23.4 kW) and the center line profiles in Figure 10, the periodic movement of bubbles through the liquid flow can be assumed, which is also described as plug flow. Regarding the curve at the length L = 2.75 m (black line) and the heat flow rate Q = 15.3 kW, the void fraction displays the same plug flow behavior as described with a maximum value of 0.415. At the higher heat flow rates, the formation of a plateau within the maximum values is visible, whereas the maximum void fraction and the duration of the plateau increase with increasing heat flow rate. This described temporal behavior and the center line void fraction profiles in Figure 10, which display that steam occupies more than half of the cross-sectional area, indicate slug flow. The curve at the length L = 3.75 m (green line) and the heat flow rate Q = 15.3 kW shows a similar course. Regarding higher heat flow rates, the tube is continuously filled with steam, what is also indicated in Figure 10. On this account, the development of a stratified wavy flow at the end of the tube can be assumed. Table 6 gives an overview of the identified flow patterns according to their axial location inside the tube and the corresponding heat transfer rate.

Table 6: Overview of the identified flow pattern assigned to their axial location inside the tube and the heat transfer rate

flow pattern	length	heat transfer rate Q
nucleate boiling	0.75 m	15.3 kW
		19.9 kW
		23.4 kW
plug flow	1.75 m	15.3 kW
		19.9 kW
		23.4 kW
	2.75 m	15.3 kW
slug flow	2.75 m	19.9 kW
		23.4 kW
	3.75 m	15.3 kW
stratified wavy flow	3.75 m	19.9 kW
		23.4 kW

Although the flow pattern has a strong influence on the heat transfer [20], ATHLET does not distinguish between flow patterns regarding the selection of the applied heat transfer correlations. Table 7 in appendix C gives an overview of the selection process for the heat transfer correlation in ATHLET. The selective parameter are the enthalpy quality x_h and the void fraction α [16].

To continue the analysis of the heat transfer, the azimuthal heat transfer coefficient h is provided with the presented experimental data according to Eq. (3) based again on the assumption of a uniform heat flux distribution inside the steam chamber to enable the application of the linear heat flow q'. Additional variables are the inner tube diameter D_i, the inner wall temperature $T_{w,i}$ and the bulk fluid temperature T_f.

$$q' = h\,\pi\,D_i\,(T_{w,i} - T_f) \tag{3}$$

The curves of this local experimental heat transfer coefficient over the tube angle are presented in Figure 12.

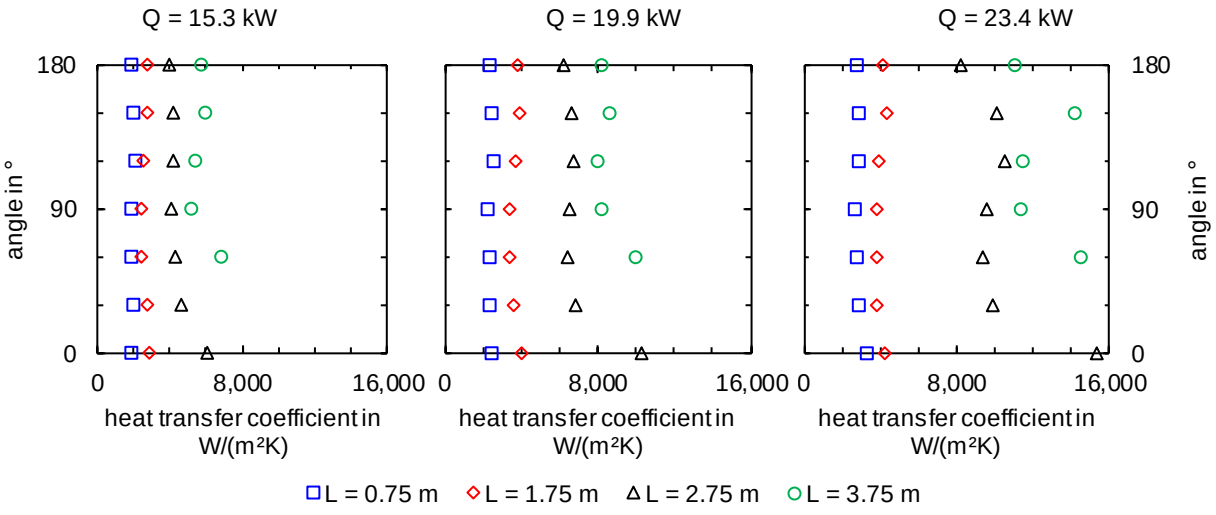

Figure 12: Heat transfer coefficient dependent on the tube angle at different axial positions for the experimental points 1 (left), 2 (middle) and 3 (right)

The diagrams show that the heat transfer coefficient increases with further distance from the tube inlet. Regarding the front half of the tube (L = 0.75 m and L = 1.75 m), the heat transfer coefficient is distributed uniformly over the circumferential angle. With further distance from the tube inlet, an azimuthal profile evolves, where the heat transfer coefficient strongly increases from the lower half of the tube. Because of the negative temperature difference between the inner wall and fluid (cf. Figure 9), the heat transfer coefficient at the angles 0° and 30° are unavailable in the diagrams.

Since for this investigation the applied system code ATHLET is a one-dimensional lumped parameter code, the heat transfer coefficient is azimuthally-averaged for the further analysis. This heat transfer coefficient is provided by applying Eq. (3) with the azimuthally-averaged inner wall temperature [21]. Figure 13 shows the development of the azimuthally-averaged heat transfer coefficient with the tube lengths for the experimental points according to Table 4.

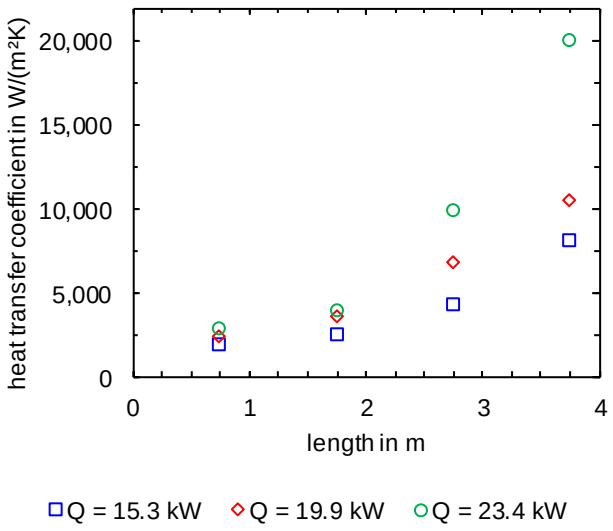

Figure 13: Development of the azimuthally-averaged heat transfer coefficient with the tube length for the experimental points 1, 2 and 3

The displayed axial courses of the heat transfer coefficient in Figure 13 base again upon the assumption of a uniform heat flux rate. The diagram reveals that the heat transfer coefficient increases in axial direction and also with increasing heat flow rate. In particular, the heat transfer coefficient at the end of the tube at a heat flow rate of 23.4 kW shows a relatively high value of about 20,034 W/(m²K).

3.2 Comparison between the experimental and computational results

As already stated in section 2.2, the measured outer wall temperatures are applied as boundary condition in the simulation. The purpose of this boundary condition is to neglect an influence on the heat input due to an insufficient prediction of the condensation heat transfer at the outside of the tube. The diagram in Figure 14 displays the experimental and simulated outer wall temperature at different axial positions.

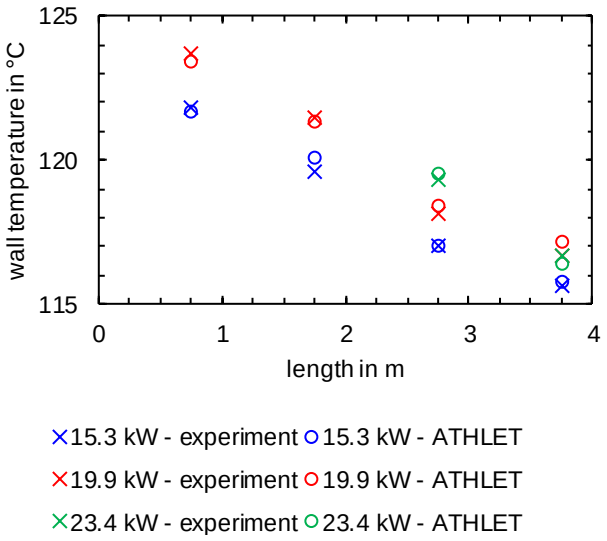

Figure 14: Comparison of the experimental and simulated axial profile of the outer wall temperature

The comparison in Figure 14 shows a sufficient agreement between the temperature in the experiments and simulations. On this account, an acceptable reproduction of the conditions in the steam chamber is assumed.

To analyze the heat transfer phenomena inside the heat transfer tube of the test facility, the bulk fluid temperature within the experiments and the simulation are compared (cf. Figure 15). For a better classification, the saturation temperature in the simulation is also presented in the diagrams. The experimental and simulated bulk fluid temperatures at the three experimental points according to Table 4 agree sufficiently till the fluid temperature reaches the saturation temperature.

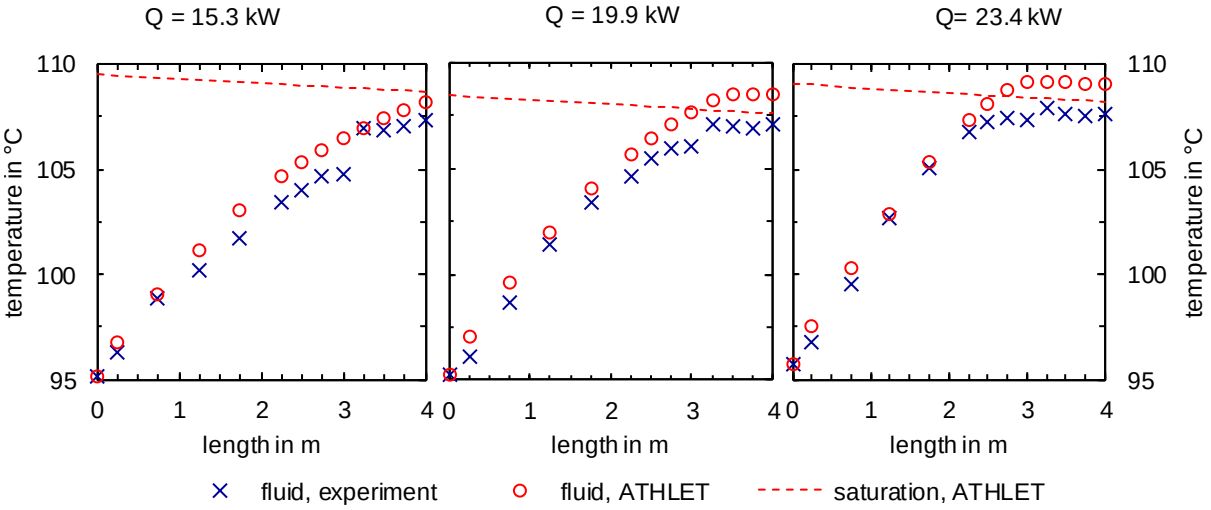

Figure 15: Comparison of the experimental and simulated axial profile of the bulk fluid temperature as well as the simulated saturation temperature for the experimental points 1 (left), 2 (middle) and 3 (right)

Since the experimental temperature course reaches the plateau at lower temperatures, a different development of the saturation temperatures between experiment and simulation can be assumed. One reason could be an insufficient calculation of the pressure drop along the tube caused by the increase of the geodetic level, of the flow resistance or of the void fraction. This difference within the saturation temperature influences the nucleation of steam and

consequently the void fraction. This impact is presented in Figure 16, which shows the development of the void fraction with the tube length in the experiment and simulation at the three provided experimental points.

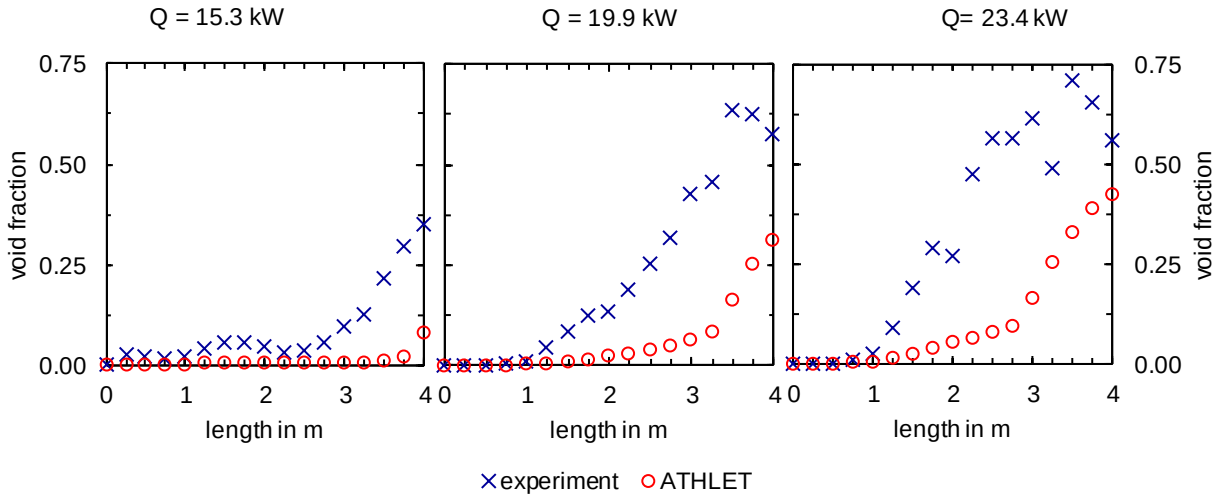

Figure 16: Comparison of the experimental and simulated axial void fraction profile for the experimental points 1 (left), 2 (middle) and 3 (right)

The diagrams in Figure 16 present significant differences not only concerning the beginning of steam nucleation inside the tube but also regarding the amount of steam. One reason is the already mentioned difference between the saturation temperature in the experiment and simulation. Another considerable influence is the constitution of the applied system code. Since the code is one-dimensional (cf. section 2.2), spatial phenomena and stratification effects within a cross-section are unable to be simulated. But Figure 7 shows a notable profile of the inner wall temperature and thus of the heat input in the cross-section especially at the end of the tube during the experiments. In order to get comparable results, the diagrams in Figure 16 compare the cross-sectionally averaged (cf. section 2.1) void fraction.

However, the void fraction has a significant influence because the heat transfer between the tube wall and the liquid phase is higher than between the tube wall and the gas phase, which in turn can affect the heat removal of the whole system. The diagram in Figure 17 compares the axial profile of the heat transfer coefficient in the experiments and the simulation.

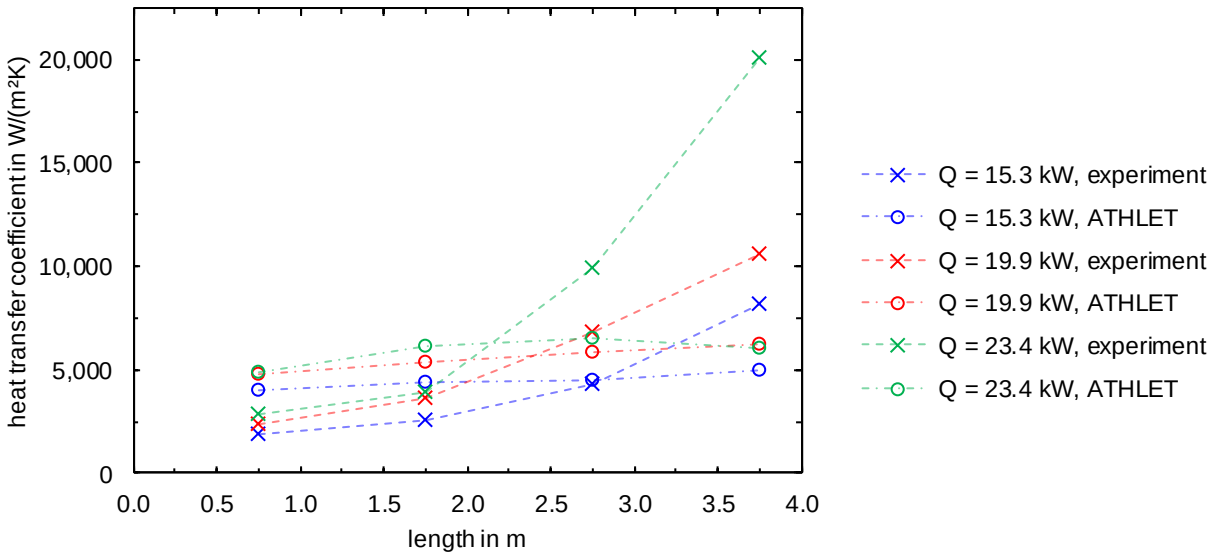

Figure 17: Comparison of the experimental and simulated axial profile of the heat transfer coefficient for the different experimental points

The experimental heat transfer coefficient is provided according to Eq. (3) assuming a uniformly distributed heat flow rate. Regarding the development of the heat transfer coefficient, different courses between experiment and simulation are noticeable. Whereas the heat transfer coefficient in the simulation slightly increases and then stays on a nearly continuous level, the experimental heat transfer coefficient shows an exponential slope. This leads to great differences at the tube outlet. Regarding the experimental point with the lowest heat flow rate (Q = 15.3 kW), the difference is already about 3,200 W/(m²K) (approx. 60%). In the experiments with the highest heat flow of 23.4 kW, the experimental heat transfer coefficient (approx. 20,000 W/(m²K)) is even more than three times higher than the heat transfer coefficient in the simulation (approx. 6,000 W/(m²K)).

4 Conclusion

To enable the safe application of passive systems for safety-related functions in nuclear reactors, an accurate and reliable prediction of the removable heat flow is crucial. Since passive containment cooling systems, which embody the last link in the heat removal chain, operate at different parameters than the validity range of established heat transfer correlations, this requirement is not accomplished.

On this account, experiments at the test facility GENEVA are performed to analyze the heat transfer during the two-phase flow development in a LPLF natural circulation system generically. By reference to the performed experiments, wall and bulk fluid temperature profiles as well as void fraction profiles and flow patterns can be determined. Moreover, conclusions regarding the local and global heat transfer coefficient are possible.

These experimental data are available to validate the mentioned heat transfer correlations. For this, a simulation with the system code ATHLET is applied, because this code offers a wide range of established heat transfer correlations. The performed simulations base upon experimental data. Furthermore, these data serve as reference for the subsequent comparison.

Regarding this comparison, the system code is not able to reproduce the experiments sufficiently. Although only a small difference between the experimental and simulated bulk fluid

temperatures is noticeable, the lower plateau at the end of the tubes in the experiments indicates a lower saturation temperature, which affects the thermal-hydraulic behavior in LPLF natural circulation systems significantly. This influence is noticeable within the void fraction profiles. In general, ATHLET computes the beginning of steam nucleation later and lower than in the experiments. These differences affect as well the development of the heat transfer coefficient, which is the actual parameter of investigation. The comparison shows enormous differences between the experimental and simulated heat transfer coefficient not only regarding the quantitative values but also considering the qualitative courses. This suggest the assumption that the applied code with the implemented correlations is unable to define the removable heat flow of such a system accurately and reliably.

On this account, heat transfer correlations have to be advanced within the range of LPLF natural circulation systems. Because of the presented data, heat transfer correlations on the basis of the occurring flow pattern is useful. Therefore, the extension of flow pattern maps regarding the range of low pressure systems is advised.

5 Acknowledgement

This work is part of the research project “PANAS” and is funded by the German Federal Ministry of Education and Research (BMBF) under the contract number 02NUK041A. Responsibility for the content of this publication lies with the authors.

6 References

[1] International Atomic Energy Agency, IAEA-TECDOC-1624: Passive Safety Systems and Natural Circulation in Water Cooled Nuclear Power Plants, Wien, 2009.

[2] R. Manthey et al., Intensive literature review of Passive Heat Removal Systems: Part II

[3] J.C. Chen, Correlation for Boiling Heat Transfer to Saturated Fluids in Convective Flow, Industrial & Engineering Chemistry Process Design and Development 5 (3) (1966), pp. 322–329.

[4] R.L. Sani: *Downflow boiling and nonboiling heat transfer in a uniformly heated tube*. Berkeley, U.S.A., University of California, Lawrence Radiation Laboratory. Master thesis. 1960 – Last access: 2018-11-19

[5] V.E. Schrock, L.M. Grossman, Forced Convection Boiling in Tubes, Nuclear Science and Engineering 12 (4) (1962), pp. 474–481.

[6] R.M. Wright: *Downflow forced-convection boiling of water in uniformly heated tubes*. Berkeley, U.S.A., University of California, Lawrence Radiation Laboratory. Dissertation. 1961 – Last access: 2018-11-19

[7] W.H. McAdams, Heat Transmission, 2 ed., McGraw-Hill Book Company Inc., New York and London, 1942.

[8] F.W. Dittus, L.M.K. Boelter, Heat transfer in automobile radiators of the tubular type, University of California Publications in Engineering 13 (2) (1930), pp. 443–461.

[9] F.H. Morris, W.G. Whitman, Heat Transfer for Oils and Water in Pipes, Industrial and Engineering chemistry (20) (1928), pp. 234–240.

[10] D.M. McEligot, T.B. Swearingen, Prediction of wall temperatures for internal laminar heat

transfer, International Journal of Heat and Mass Transfer (1966), pp. 1151–1152.

[11] W.M. Kays, W.B. Nicoll, Laminar Flow Heat Transfer to a Gas With Large Temperature Differences, Journal of Heat Transfer (85) (1963), pp. 329–338.

[12] T. Cloppenborg, C. Schuster, A. Hurtado, Two-phase flow phenomena along an adiabatic riser – An experimental study at the test-facility GENEVA, International Journal of Multiphase Flow 72 (2015), pp. 112–132.

[13] H.-M. Prasser, A. Böttger, J. Zschau, A new electrode-mesh tomograph for gas–liquid flows, Flow Measurement and Instrumentation 9 (2) (1998), pp. 111–119.

[14] M. Beyer et al., Wire-Mesh Sensor Data Processing Software: User Manual and Software Description

[15] E. Schleicher et al., Measurement of two-phase flow parameters with multi-channel gamma densitometry and local void probes at the INKA test facility, in: Canadian Nuclear Society (Ed.), Proceedings of the 14th International Topical Meeting on Nuclear Reactor Thermalhydraulics, 2011.

[16] Gesellschaft für Anlagen- und Reaktorsicherheit (GRS) gGmbH, ATHLET 3.1A: Models and Methods, 2016.

[17] Gesellschaft für Anlagen- und Reaktorsicherheit (GRS) gGmbH, ATHLET 3.1A: Validation, 2016.

[18] S. Buchholz, D. von der Cron, A. Schaffrath, System code improvements for modelling passive safety systems and their validation, Kerntechnik 81 (5) (2016), pp. 535–542.

[19] P. Schöffel et al., Weiterentwicklung des Systemrechenprogramms ATHLET für Anwendungen in der Reaktorsicherheit: Im Rahmen des EU-Projekts THINS: Abschlussbericht, Köln.

[20] D. Steiner, Strömungssieden gesättigter Flüssigkeiten, in: Verein Deutscher Ingenieure, VDI-Gesellschaft Verfahrenstechnik und Chemie-ingenieurwesen (Eds.), VDI-Wärmeatlas, 10. Aufl., Berlin, Heidelberg, Springer Verlag Berlin Heidelberg, 2006, Hbb1-Hbb35.

[21] W. Bonn et al., Über die Auswirkungen der Ungleichverteilung des Wärmeübergangs am Rohrumfang bei der Verdampfung im durchströmten waagerechten Rohr, Wärme- und Stoffübertragung 13 (4) (1980), pp. 265–274.

Symbols

Latin

A	area in m²
c	chord length in m
c_p	specific heat at constant pressure in J/(kgK)
D	hydraulic diameter in m
Gr	Grashof number
H	sagitta of the segment in m
h	heat transfer coefficient in W/(m²K)
I	raw data
$\bar{I}$	time-averaged data
i_{fg}	latent heat in J/kg
k	heat conductivity in W/(mK)
L	length in m
$\dot{m}$	mass flow in kg/s

Greek

α	void fraction
γ	inclination angle in °
ϑ	temperature in °C
μ	dynamic viscosity in kg/(ms)
ν	kinematic viscosity in m²/s
ρ	density in kg/m³
σ	surface tension in N/m

Indices

f	fluid
g	gas
i	inner
l	liquid

Pr	Prandtl number
ΔP	critical pressure difference
p	pressure in bar
Q	rate of heat flow in W
q'	linear heat flux in W/m
Re	Reynolds number
S	suppression factor
s	arc length in m
T	temperature in K
X_{tt}	Martinelli number
x	quality
x_h	enthalpy quality

lam	laminar
$meas$	measured
o	outer
sat	saturation
seg	segment
st	steel
$turb$	turbulent
w	wall
$water$	water
x	probe position
y	height
z	frame

7 Abbreviations

approx.	approximately
ATHLET	analysis of thermal-hydraulics of leaks and transients
CV	control volumes
e. g.	example given
ESBWR	economic simplified boiling water reactor
LPLF	low pressure and low flow
SBWR	simplified boiling water reactor
TFO	thermo-fluiddynamic object

Appendix A

$$h_{ModifiedChen} = 0.023\,\frac{k_l}{D}\,Re_l^{0.8}\,Pr_l^{0.4}\,(1 + 1.6\,\mathrm{X_{tt}^{0.8174}}) + 0.00122\,\frac{k_l^{0.79}\,c_{p,l}^{0.49}\,\rho_l^{0.49}}{\sigma_l^{0.5}\,\mu_l^{0.29}\,i_{fg}^{0.24}\,\rho_g^{0.24}}\,\frac{(T_w - T_{sat})^{1.24}}{T_w - T_l}\,\Delta P^{0.75}\,S \quad \textbf{(4)}$$

with

$$\Delta P = \frac{i_{fg}\,(T_w - T_{sat})}{(v_g - v_l)\,T_{sat}}$$

$$S = \begin{cases} \dfrac{1+\cos\gamma}{2}\,S_0 + \left(1 - \dfrac{1+\cos\gamma}{2}\right) S_0 & ,\text{if } 0° \le \gamma < 90° \\ 1 & ,\text{if } \gamma = 90° \end{cases}$$

$$S_0 = \begin{cases} [1 + 1.63\cdot 10^{-5}\,Re_l(1-x_h)(1+1.6\,\mathrm{X_{tt}^{0.8174}})^{1.25}]^{-1} & ,\text{if } Re_l(1-x_h)(1+1.6\,\mathrm{X_{tt}^{0.8174}})^{1.25} < 4\cdot 10^5 \\ 0.133 - 0.825\cdot 10^{-7}[Re_l(1-x_h)(1+1.6\,\mathrm{X_{tt}^{0.8174}})^{1.25} - 4\cdot 10^5] & ,\text{if } Re_l(1-x_h)(1+1.6\,\mathrm{X_{tt}^{0.8174}})^{1.25} \ge 4\cdot 10^5 \end{cases}$$

$$h_{McAdams,l} = 0.15\frac{k_l}{D}\,(Gr_l\,Pr_l)^{0.33}[1 + (2\,Pr_l)^{-0.5625}]^{-0.5926} \quad \textbf{(5)}$$

$$h_{McAdams,g} = 0.13\frac{k_g}{D}\,\left(Gr_g\,Pr_g\right)^{0.33} \quad \textbf{(6)}$$

$$h_{Dittus-Boelter} = 0.023\,\frac{k_g}{D}\,Re_g^{0.8}\,Pr_g^{0.4} \quad \textbf{(7)}$$

$$h_{McEligot} = 0.021\,\frac{k_g}{D}\,Re_g^{0.8}\,Pr_g^{0.4}\,\left(\frac{T_g}{T_w}\right)^{0.5} \quad \textbf{(8)}$$

Appendix B

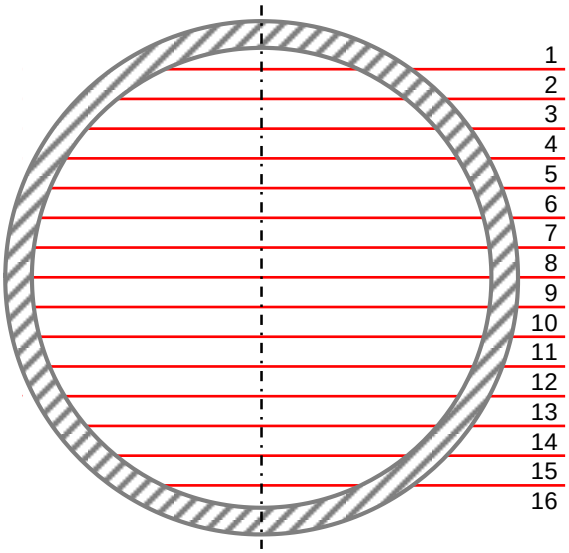

Figure 18: Division of the tube cross-section into circular segment areas according to the measuring points of the void probes

$$c = 2\cdot\sqrt{D\cdot H_y - H_y^2} \quad \textbf{(9)}$$

$$s = D\cdot\arcsin\left(\frac{c}{D}\right) \quad \textbf{(10)}$$

$$A_{seg,y} = \frac{D\cdot s}{4} - \frac{c\cdot(0.5\,D - H_y)}{2} \quad \textbf{(11)}$$

$$A_y = \begin{cases} A_{seg,y} - A_{seg,y-1} & ,\text{if } y \le 8 \\ A_{seg,y} - A_{seg,y+1} & ,\text{if } y > 8 \end{cases} \quad \textbf{(12)}$$

Appendix C

Table 7: Overview selection process for the heat transfer correlations in ATHLET for heat flow from wall to fluid (natural and forced convection, subcooled and saturated nucleate boiling) [16]

condition	mode	applied correlation
$x_h \leq -0{,}05$	21	$h = \max\left(h_{ModifiedChen}, h_{NaturalConvection,liquid}, 20\frac{W}{m^2K}\right)$
$-0{,}05 \leq x_h < 0$	22	$h = \frac{1+\cos(x_h \cdot \pi)}{2} \cdot h_{21} + \left(1 - \frac{1+\cos(x_h \cdot \pi)}{2}\right) \cdot h_{25}$
$x_h \geq 0$ $\alpha \leq 0{,}97$	25	$h = \max\left(h_{ModifiedChen}, h_{NaturalConvection,liquid}, 20\frac{W}{m^2K}\right)$
$0{,}97 < \alpha < 0{,}985$	26	$h = \frac{1+\cos(\alpha \cdot \pi)}{2} \cdot h_{25} + \left(1 - \frac{1+\cos(\alpha \cdot \pi)}{2}\right) \cdot h_{29}$
$\alpha \geq 0{,}985$	29	$h = \max(h_{turb}, h_{lam})$ with $h_{turb} = \begin{cases} h_{DittusBoelter,steam} & \text{, if stable film boiling occurs} \\ h_{McEligot} & \text{, if pool film boiling occurs} \\ h_{PebbleBed} & \text{, if the heat transfer geometry is spherical} \end{cases}$ $h_{lam} = \max\left(h_{NaturalConvection}, h_{Hausen}, 10\frac{W}{m^2K}\right)$